

A multiband electronic characterization of the complex intermetallic cage system $Y_{1-x}Gd_xCo_2Zn_{20}$

M. Cabrera-Baez,¹ A. Naranjo-Uribe,² J. M. Osorio-Guillén,² C. Rettori,^{1,3} and M. A. Avila¹

¹CCNH, Universidade Federal do ABC (UFABC), Santo André, SP, 09210-580 Brazil

²Instituto de Física, Universidad de Antioquia UdeA, Calle 70 No 52-21, Medellín, Colombia

³Instituto de Física “Gleb Wataghin”, UNICAMP, Campinas, SP, 13083-859 Brazil

(Dated: December 7, 2024)

A detailed microscopic and quantitative description of the electronic and magnetic properties of Gd^{3+} -doped YCo_2Zn_{20} single crystals ($Y_{1-x}Gd_xCo_2Zn_{20}$: $0.002 \lesssim x \leq 1.00$) is reported through a combination of temperature-dependent Electron Spin Resonance (ESR), heat capacity and *dc* magnetic susceptibility experiments, plus first-principles Density Functional Theory (DFT) calculations. The ESR results indicate that this system features an *exchange bottleneck* scenario wherein various channels for the spin-lattice relaxation mechanism of the Gd^{3+} ions can be identified via exchange interactions with different types of conduction electrons at the Fermi level. Quantitative support from the other techniques allow to extract the exchange interaction parameters between the localized magnetic moments of the Gd^{3+} ions and the different types of conduction electrons present at the Fermi level (J_{fs} , J_{fp} and J_{fd}). Despite the complexity of the crystal structure, our combination of experimental and electronic structure data establish $GdCo_2Zn_{20}$ as a model Ruderman-Kittel-Kasuya-Yosida (RKKY) system by predicting a Curie-Weiss temperature $\theta_C = -1.2(2)$ K directly from microscopic parameters, in very good agreement with the bulk value from magnetization data. The successful microscopic understanding of the electronic structure and behavior for the two end compounds YCo_2Zn_{20} and $GdCo_2Zn_{20}$ means they can be used as references to help describe the more complex electronic properties of related materials.

PACS numbers: 76.30.-v, 71.20.-b, 76.60.Es

I. INTRODUCTION

The understanding of the physical properties of complex materials with cage-like structures, such as the family RT_2Zn_{20} (R = rare earth, T = transition metal), have attracted the attention of many researchers focused in condensed matter physics. Among other aspects, these intermetallic cage compounds generate interest due to the different types of electronic and magnetic behaviors governed by “naturally diluted” rare earth ions.^{1,2} The magnetic versatility associated with the $4f$ electrons goes from weakly correlated Pauli-like paramagnetic behavior (Lu^{3+}), to hybridization with conduction electrons (Yb^{3+}) and peculiar interactions of local magnetic moments (Gd^{3+}) with conduction electrons, as a few examples.

Despite the apparent complexity (184 atoms per conventional unit cell arranged in different types of cages), their crystallographic structure can be broken down into surprisingly simple sub-units, which allows clean analyzes and interpretations of experimental results, and sets this family as an excellent model system for several physical problems. They adopt a cubic $CeCr_2Al_{20}$ -type structure (space group: $Fd\bar{3}m$),³ in which the R and T ions occupy their own unique crystallographic sites ($8a$ and $16d$, respectively). The Zn ions form the cage structure by occupying three inequivalent crystallographic sites ($96g$, $48f$ and $16c$). If we consider the sub-structure in terms of the nearest neighbors and the next nearest neighbors, the R and T ions are fully surrounded by shells formed by Zn ions, leaving a shortest R-R spacing of $r \approx 6 \text{ \AA}$. The R

ions are thus isolated in a Frank-Kasper cage formed by 16 Zn ions as exemplified in Fig. 1.

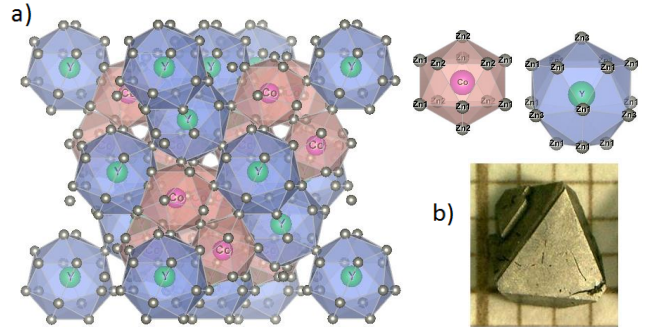


FIG. 1: (a) The cubic unit cell of the YCo_2Zn_{20} , the CN-16 Frank-Kasper polyhedron of rare earth ions and the polyhedron of transition metal ions. (b) Typical crystal of YCo_2Zn_{20} showing a [111] triangular facet.

The observation of radically different magnetic behaviors such as the contrast between low-temperature anti-ferromagnetic order ($T_N \sim 5.7$ K) in $GdCo_2Zn_{20}$ ⁴ and the high temperature ferromagnetic order ($T_C \sim 86$ K) in $GdFe_2Zn_{20}$ ⁴ hints at peculiar magnetic couplings governed by the Ruderman-Kittel-Kasuya-Yosida (RKKY) interaction. In the case of Y-based compounds, strongly different types of behavior are also found. YFe_2Zn_{20} has been described as a “nearly ferromagnetic Fermi sea” compound⁵ because it is near the Stoner limit, in contrast to YCo_2Zn_{20} with more conventional metallic behavior.

Moreover, within this family all the Yb-based compounds described so far have presented heavy fermion behavior,⁶ as evidenced by the enhanced Sommerfeld coefficients, such as $\text{YbCo}_2\text{Zn}_{20}$ with $\gamma \approx 7900 \text{ mJ/mol K}^2$. All of these observations point to the need to investigate the electronic structure⁷, particularly around the Fermi level, and describe the electronic interactions in detail to better understand the electronic and magnetic behaviors.

In order to conduct this task in a controllable manner, we have chosen an initial focus on the weakly correlated compound $\text{YCo}_2\text{Zn}_{20}$ that features Pauli like paramagnetism, metallic transport and a Sommerfeld coefficient of $\gamma \approx 18 \text{ mJ/mol K}^2$,^{2,4} as an appropriate host for a microscopic study using Gd^{3+} ions as an electron spin resonance (ESR) probe. ESR of rare earth ions diluted in metallic hosts is a useful local technique to investigate microscopic properties of materials, since it directly probes the localized magnetic moments and the nature of the interactions with their neighbors.^{8,9} The metallic and nonmagnetic $\text{YCo}_2\text{Zn}_{20}$ host doped with Gd is an excellent model system to study the Gd^{3+} spin-lattice relaxation, associated with the conduction electrons (*ce*) spin-flip scattering mechanism due to the exchange interaction between the localized magnetic moment and the *ce*. The Hasegawa-Korringa model^{10,11} for the spin-lattice relaxation has been carefully discussed and applied in previous studies of ESR for Gd^{3+} in the intermetallic compounds like LaAl_2 ¹², LuAl_2 ¹³ and in elemental Al.¹⁴ We have recently applied the same technique to investigate the electronic structure of the superconductor YIn_3 .¹⁵

In this work we show that the ESR spectra of Gd^{3+} in $\text{YCo}_2\text{Zn}_{20}$ ($0.001 \lesssim x \leq 1.00$) presents a Gd^{3+} concentration- dependent thermal broadening of the linewidth and *g*-shift. This reveals the existence of the exchange *bottleneck* effect in this compound, that can be tuned by the concentration of Gd^{3+} . By combining the ESR results with heat capacity, magnetic susceptibility and band structure calculations, we extract the exchange parameters of the interaction between Gd^{3+} and the *s*, *p*, and *d ce* present at the Fermi level of $\text{YCo}_2\text{Zn}_{20}$. We are then able to establish a clear correlation of these microscopic parameters with the RKKY interaction. This in turn offers a better understanding of the peculiar “Fermi sea” present in the system, which has lead to the magnetic anomalies found in this family.

II. EXPERIMENTAL AND COMPUTATIONAL DETAILS

Batches of $\text{Y}_{1-x}\text{Gd}_x\text{Co}_2\text{Zn}_{20}$ ($0.001 \lesssim x \leq 1.00$) single crystals were grown by the self-flux method^{16,17} using excess Zn. The starting reagents were 99.9% Y, 99.9% Co, 99.9% Gd and 99.9999% Zn (Alfa-Aesar). Initial ratios of elements were 1:2:47 for the pure ternaries Y:Co:Zn and Gd:Co:Zn, or 1-x:x:2:47 for the pseudo-quaternaries Y:Gd:Co:Zn. The elemental mixtures were sealed in an evacuated quartz ampoule and placed in a box furnace

for the temperature ramping. Crystals were grown by slowly cooling the melt between 1100 °C and 600 °C over 100 h. At 600 °C the ampoules were removed from the furnace, inverted and placed in a centrifuge to spin off the excess flux. The separated crystals are typically polyhedral, $\sim 3 \text{ mm}$ or larger and manifest clear, triangular [111] facets (Fig. 1). The Gd concentrations were estimated based on the effective moments per formula unit extracted from fits of magnetic susceptibility measurements. Powder x-ray diffraction on crushed crystals was used to ascertain the $\text{CeCr}_2\text{Al}_{20}$ -type structure³ as exemplified for $\text{YCo}_2\text{Zn}_{20}$ in Fig. 2. The refined lattice parameter of $a = 14.042(4) \text{ \AA}$ is in good agreement with the literature.¹ The inset shows that the refined lattice parameter increases linearly with Gd concentration, as expected by Vegard’s law.¹⁸

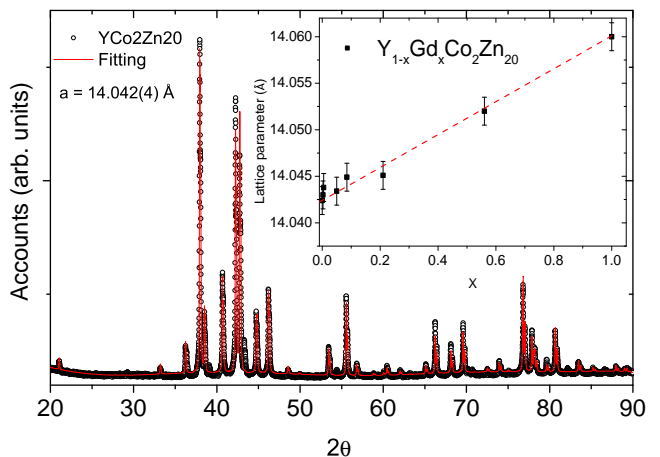


FIG. 2: XRD pattern of $\text{YCo}_2\text{Zn}_{20}$. Inset, Lattice parameter for the $\text{Y}_{1-x}\text{Gd}_x\text{Co}_2\text{Zn}_{20}$ ($0.001 \lesssim x \leq 1.00$) compounds.

For the ESR experiments, single crystals were crushed into fine powders of particle size greater than $100 \mu\text{m}$, corresponding to average grain size (*d*) larger than the skin depth (δ), $\lambda = d/\delta \gtrsim 10$. We have noticed that experiments on as-grown single crystals should be carried out with caution, because strong resonances similar to those reported by Ivanshin *et al.*¹⁹ are frequently observable, and likely due to residual Co surface contamination since that particular signal disappears after removing the as-grown crystal surfaces. The X-Band ($\nu \approx 9.4 \text{ GHz}$) ESR experiments were carried out in a conventional CW Bruker-ELEXSYS 500 ESR spectrometer using a TE_{102} cavity. The sample temperature was changed using a helium gas-flux coupled to an Oxford temperature controller. The specific heat (C_p) and magnetic susceptibility ($\chi = M/H$) measurements were performed on Quantum Design PPMS and SQUID-VSM platforms, respectively, using their standard procedures.

The ground state crystal structures were calculated using spin-polarized first-principles DFT, with the PBEsol exchange-correlation functional.²⁰ The Kohn-Sham equa-

tions were solved using the projector augmented plane-wave (PAW) method as implemented in the VASP code.^{21,22} The PAW atomic reference configurations are: $4s^2 4p^6 4d^1 5s^2$ for Y, $5s^2 5p^6 4f^7 5d^1 6s^2$ for Gd, $3s^2 3p^6 3d^7 4s^2$ for Co and $3p^6 3d^{10} 4s^2$ for Zn, where only electrons treated as valence electrons are explicitly enumerated. The energy cut-off in the plane-waves expansion is 507.5 eV, where the total energy has been converged to 1 meV/unit cell. All structural parameters, lattice constants and atomic positions for each calculated compound have been optimized by simultaneously minimizing all atomic forces and stress tensor components via a conjugate gradient method. Successive full-cell optimizations adapting basis vectors have been conducted until the unit cell energies and structural parameters have been fully converged. Brillouin-zone integration has been performed on a Monkhorst-Pack $12 \times 12 \times 12$ -k-mesh with a Gaussian broadening of 0.01 eV for full relaxation (ionic forces are converged to 0.1 meV/Å). Then, we used the relaxed crystal structures to calculate the total and partial density of states (DOS), the dispersion relations and the Fermi surfaces using the full-potential augmented-plane wave method with local orbitals.²³ The muffin-tin (MT) radii of Y, Gd, Co and Zn are set to $R_{\text{MT}} = 2.6, 2.8138, 2.2804$ and 2.2804 a.u., respectively. The parameter $R_{\text{MT}}|\mathbf{G} + \mathbf{k}|_{\text{max}}$ governing the number of plane waves has been converged to 9.0. The irreducible wedge of Brillouin zone is sampled with a uniformly spaced \mathbf{k} -grid of $20 \times 20 \times 20$. Fermi surfaces were plotted using the XCrysDen package.²⁴

III. EXPERIMENTAL RESULTS

Figure 3 displays the Gd^{3+} ESR spectra in $\text{Y}_{1-x}\text{Gd}_x\text{Co}_2\text{Zn}_{20}$ for $x \approx 0.002$ and $x \approx 0.21$ at 4.4 K and 12.5 K, respectively, and microwave power of $P_{\mu\omega} \approx 2$ mW. These ESR spectra show different resonance magnetic fields than that of Gd^{3+} in insulators, for which a resonance field of $H_0 = 3.386(4)$ Oe and g -value of 1.993(2) are well established.²⁵ It is evident that for the low concentration sample ($x = 0.002$) the resonance is shifted toward a lower field (higher g -values) compared to that of the higher concentration sample ($x = 0.21$).

The observed ESR spectra of Gd^{3+} localized magnetic moments in $\text{Y}_{1-x}\text{Gd}_x\text{Co}_2\text{Zn}_{20}$ will be analyzed according to the generally accepted approach where, at resonance, the microwave absorption in a metal is given by the Dyson theory in the diffusionless limit, $A/B \approx 2.6$.^{26,27} In this limit, for particles larger than the skin depth, the ESR spectra reduce to a simple admixture of absorption (χ'') and dispersion (χ') of Lorentzian lineshapes.^{26,27} The derivative of this admixture is given by:

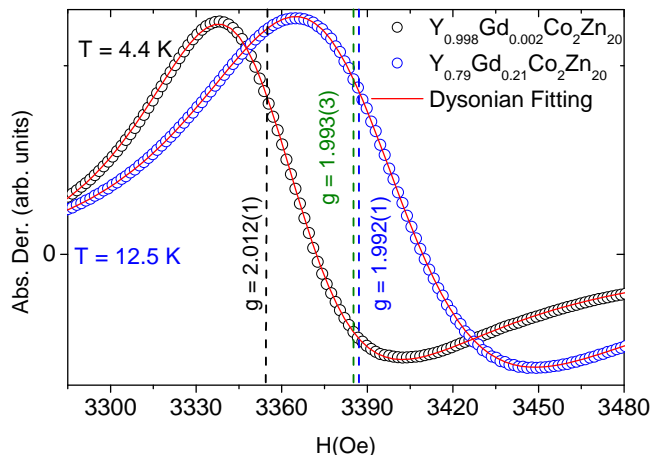


FIG. 3: Gd^{3+} ESR spectra of $\text{Y}_{1-x}\text{Gd}_x\text{Co}_2\text{Zn}_{20}$ for $x \approx 0.002$ at $T = 4.4$ K and $x \approx 0.21$ at $T = 12.5$ K for a microwave power of $P_{\mu\omega} \approx 2$ mW.

$$\frac{d[(1-\alpha)\chi'' + \alpha\chi']}{dH} = \chi_0 H_0 \gamma_e^2 T_2^2 \left[\frac{2(1-\alpha)x}{(1+x^2)^2} + \frac{\alpha(1-x^2)}{(1+x^2)^2} \right] \quad (1)$$

$$x = (H_0 - H) \gamma_e T_2,$$

where H_0 and H are the resonance and the applied fields respectively, γ_e is the electron gyromagnetic ratio, T_2 the spin-spin relaxation time, α the admixture of absorption ($\alpha = 0$) and dispersion ($\alpha = 1$) and χ_0 the paramagnetic contribution from the static susceptibility. It is usually accepted²⁷ that for diluted magnetic moments in a metallic host $T_1 \approx T_2$, where T_1 is the spin-lattice relaxation time.^{25,28} Therefore, the fitting of the experimentally observed ESR absorption lines to Eq. 1 allows the extraction of the two most relevant ESR parameters, i.e., the g -value from the resonance condition, $h\nu = g\mu_B H_0$, and the linewidth $\Delta H = 1/\gamma_e T_2$.

Figure 4 displays the T -dependence of the Gd^{3+} ESR linewidth, ΔH , in $\text{Y}_{1-x}\text{Gd}_x\text{Co}_2\text{Zn}_{20}$ for $0.002 \lesssim x \lesssim 1.00$ at a microwave power of $P_{\mu\omega} \approx 2$ mW. The broadening of ΔH at low temperature for the high concentration samples is presumably originated by the interaction between randomly distributed Gd^{3+} magnetic moments, that cause an inhomogeneous local field. However, for the stoichiometric $\text{GdCo}_2\text{Zn}_{20}$ this disorder should be absent and the low temperature broadening of ΔH less pronounced (see Fig. 4). This allows the drop in the magnetic susceptibility at T_N to become evident in the ESR intensity (see Fig. 7). The high T -dependence of ΔH follows the linear behavior $\Delta H = a + bT$ where the a parameter represents the residual linewidth, ΔH_0 , and $b = d(\Delta H)/dT$ the Korringa-like relaxation rate. The extracted a and b values are given in Table I, together with the obtained g -values at $T \approx 10$ K for the studied

samples.

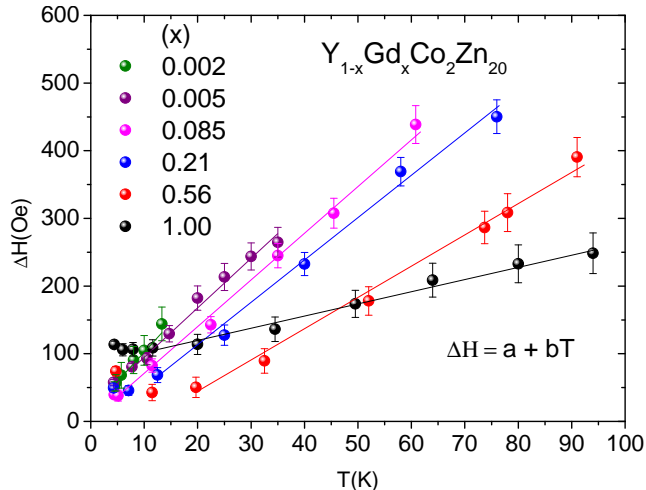


FIG. 4: T -dependence of the Gd^{3+} ESR linewidth, ΔH , in $\text{Y}_{1-x}\text{Gd}_x\text{Co}_2\text{Zn}_{20}$ for $0.001 \lesssim x \lesssim 1.00$.

Figure 5 displays the Gd concentration dependence of the g -shift ($\Delta g = g - 1.993(2)$) and in the inset the thermal broadening of the linewidth, b . The general trends of the data presented in Fig. 5 is characteristic of an *exchange bottleneck* phenomenon, where the *ce* relaxation to the Gd^{3+} localized magnetic moment (Overhauser relaxation) overcomes the *ce* spin-lattice relaxation.

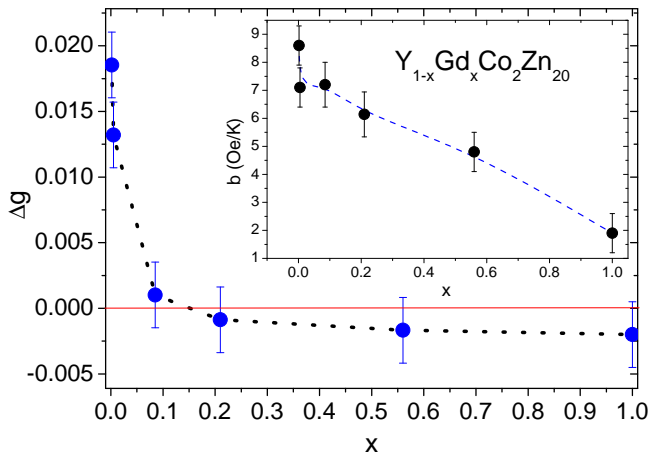


FIG. 5: Gd concentration dependence of the g -shift ($\Delta g = g - 1.993(2)$) and in the Inset the thermal broadening of the linewidth, b , for the $\text{Y}_{1-x}\text{Gd}_x\text{Co}_2\text{Zn}_{20}$ system. The dashed lines are guides for the eye.

We now focus on bulk thermodynamic measurements which, together with the band structure calculations presented in the following section, provide support for a proper quantitative analysis of the ESR results. Figure 6 shows the low temperature linear behavior of C_p/T as a function of T^2 leading to a Sommerfeld coefficient of

$\gamma \approx 18(3)$ mJ/mol K^2 and a Debye temperature of $\Theta_D = 127(5)$ K for the $\text{YCo}_2\text{Zn}_{20}$ compound. The inset of Fig. 6 zooms in on the weak T -dependence of the magnetic susceptibility, $\chi(T)$, for $\text{YCo}_2\text{Zn}_{20}$. The dome-like feature at $T \approx 120$ K may be due to T -dependent *d-ce* at the Fermi surface (see Fig. 10 below) and the small upward tail at low temperature (which has no influence in the analyzes that follow) due to residual rare-earth magnetic impurities from the 99.9% Y reagents used in our samples.

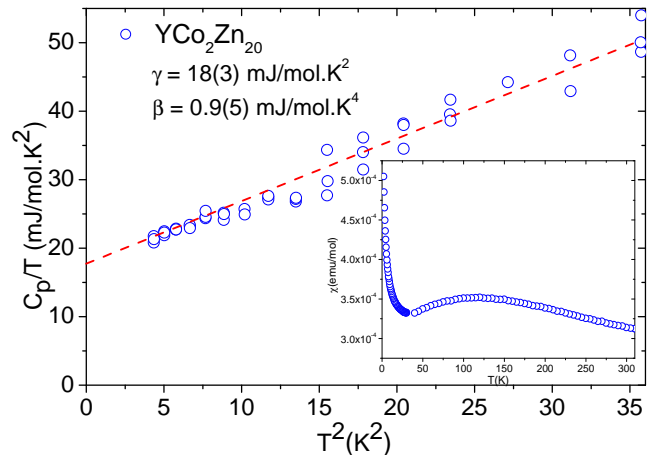


FIG. 6: Low temperature specific heat, C_p/T , showing a linear behavior with a Sommerfeld coefficient of $\gamma \approx 18(3)$ mJ/mol K^2 and a Debye temperature of $\Theta_D = 127(5)$ K for $\text{YCo}_2\text{Zn}_{20}$. The inset zooms in on the weak T -dependence of the magnetic susceptibility, $\chi(T)$, for $\text{YCo}_2\text{Zn}_{20}$

Fig. 7 presents the T -dependence of the magnetic susceptibility of $\text{GdCo}_2\text{Zn}_{20}$ where the antiferromagnetic order is seen at a Neel temperature of $T_N \approx 5.7$ K, with an effective magnetic moment $\mu_{eff} \approx 8.1(2)$ μ_B , comparable to that of Gd^{3+} ions ($\mu_{eff} = 7.94\mu_B$) and a paramagnetic Curie temperature $\theta_C \approx -1.8(3)$ K. Note that the paramagnetic Curie temperature θ_C is the same as T_C in the Weiss molecular field theory. Fig. 7 also shows that the ESR signal integrated intensity follows the trends of the magnetic susceptibility, crossing the paramagnetic-antiferromagnetic transition at approximately the same Neel temperature. This is in itself a rare observation because usually, around the ordering temperature of a magnetic transition, the ESR signal is lost due to a strong broadening of the resonance.

The magnetic susceptibility for all our $\text{Y}_{1-x}\text{Gd}_x\text{Co}_2\text{Zn}_{20}$ samples were fitted to a Curie-Weiss law using the effective magnetic moment of $\mu_{eff} = 7.94\mu_B$ for the Gd^{3+} ions. From these fittings the Gd concentrations were estimated and their values are listed in Table I.

IV. ANALYSIS AND DISCUSSION

The low- T linear behavior of $C_p/T = \gamma + \beta T^2$ for $\text{YCo}_2\text{Zn}_{20}$ of Figure 6 leads to a Sommerfeld coefficient

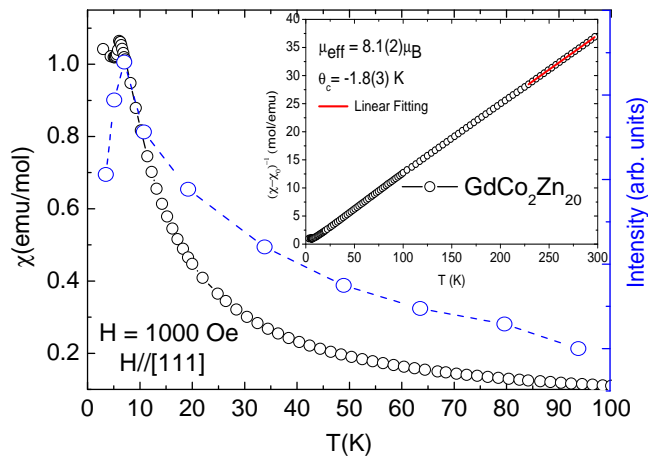


FIG. 7: T -dependence of the dc magnetic susceptibility and the Gd^{3+} ESR intensity for $\text{GdCo}_2\text{Zn}_{20}$. Both experiments show the magnetic paramagnetic-antiferromagnetic transition at $T_N \approx 5.7$ K. The inset shows the inverse magnetic susceptibility and linear fit results.

cient $\gamma = 18(3)$ mJ/mol K^2 and a Debye temperature $\Theta_D = 127(5)$ K. It is worth mentioning that low Θ_D values are not unusual in complex structures, particularly for $\text{RT}_2\text{Zn}_{20}$ compounds, where it may be influenced by the reported *rattling* of Zn ions at the $16c$ site.³⁰ In the Fermi liquid model the Sommerfeld coefficient is given by $\gamma = (2/3)\pi^2 k_B^2 \eta_F$, where η_F is the total density of states (DOS) per formula unit (f.u.), spin and eV at the Fermi level. Thus, we estimate $\eta_F = 3.8(8)$ states/f.u., spin and eV for $\text{YCo}_2\text{Zn}_{20}$.

A Pauli-like paramagnetic susceptibility for $\text{YCo}_2\text{Zn}_{20}$ can be estimated at high- T (310 K). The data in the inset of Figure 6 presents, after correction by the core diamagnetism of $\text{YCo}_2\text{Zn}_{20}$ ($\chi_{dia} = -2.3 \times 10^{-4}$ emu/mol), a magnetic susceptibility value at $T \approx 310$ K of $\chi_0 - \chi_{dia} = 0.312 \times 10^{-3}$ emu/mol which is slightly smaller than the value reported by Jia *et al.*⁵

Once again within the Fermi liquid model, the Pauli-like paramagnetic susceptibility is given by $\chi_0 = 2\mu_B^2 \eta_F$. Then, using the experimental Pauli paramagnetic susceptibility for $\text{YCo}_2\text{Zn}_{20}$ we estimate $\eta_F = 4.8(9)$ states/f.u. However, one has to consider the possibility of an exchange-enhanced magnetic susceptibility, i.e., $\chi = \chi_0 / (1 - \xi)$, where ξ accounts for the electron-electron exchange enhancement. Nevertheless, the estimated value of $\eta_F = 4.8(9)$ states/f.u is, within the accuracy of our experiments, comparable to the value obtained from the Sommerfeld coefficient. Thus, in our analysis we shall ignore the electron-electron exchange enhancement for $\text{YCo}_2\text{Zn}_{20}$.

From the high- T data of Figure 7 (250 K - 300 K) for $\text{GdCo}_2\text{Zn}_{20}$ we obtain a small negative value for the Curie temperature, $\theta_C = -1.8(3)$ K, as expected for this antiferromagnetic material. This is in contrast to the small positive value reported in previous studies which used a

TABLE I: Gd concentrations, g -values, residual linewidths, a , and thermal broadening of the linewidths, b , for the $\text{Y}_{1-x}\text{Gd}_x\text{Co}_2\text{Zn}_{20}$ system.

Conc.	g -value	Measured b	Calculated b
x	(10 K)	(Oe/K)	(Oe/K)
0.002	2.012(1)	8.6(6)	8.4(3)
0.005	2.006(1)	7.1(6)	4.3(3)
0.085	1.994(1)	7.2(6)	0.02(3)
0.21	1.992(1)	6.1(6)	0.02(3)
0.56	1.991(2)	4.8(6)	0.08(5)
1.00	1.991(2)	1.9(6)	0.09(5)

fitting range extended to lower temperatures.⁴ We argue that fitting at higher- T intervals are more appropriate to obtain an estimation of the Curie temperature with better accuracy.

In order to complement the experimental data analysis and provide details about the electronic structure, we have performed first-principles band structure calculations for the pure compounds $\text{GdCo}_2\text{Zn}_{20}$ and $\text{YCo}_2\text{Zn}_{20}$. For $\text{GdCo}_2\text{Zn}_{20}$ we have obtained that the magnetic stabilization energy $\Delta_{\text{AFM}} = E_{\text{AFM}} - E_{\text{FM}} = -2$ meV/unit cell, therefore the ground state is antiferromagnetic, with a calculated local magnetization of the two Gd ions equal to $\pm 7\mu_B$. On the other hand, $\text{YCo}_2\text{Zn}_{20}$ converged to a non magnetic ground state.

Figure 8 shows the calculated dispersion relations for these two systems. For $\text{GdCo}_2\text{Zn}_{20}$ the valence bands are built up mainly from Zn d -states and a small contribution of Zn s and p -states between -11 and -6.5 eV for both systems. The remaining of the valence bands are the result of the hybridization of Gd d and f -states, the latter localized between -3.3 and -2.8 eV, Co d -states and Zn s, p and d -states. The conduction bands are also built up from the hybridization of Gd d and f -states, Co d -states and Zn s, p and d -states, with the Gd f -states localized between 0.3 and 1 eV. On the other hand, the bands of $\text{YCo}_2\text{Zn}_{20}$ are built up similar to the previous system with the obvious absence of f -states, in this case Y d -states contribute mostly to the upper valence bands and the conduction bands. As it can be observed in Fig. 8, the topology of the bands is almost identical for the two systems especially the four conduction bands that cross the Fermi level. The similarity of these four bands is more lively appreciable in the branches of the Fermi surface, as it is seen in Fig. 9. The first branch is formed by eight pockets along the Q direction of the first Brillouin zone, these pockets are formed from the contributions of Gd(Y) d -states and Co d -states. The second branch of the Fermi surface has eight connected structures along the Δ, V, Q and Λ directions that resemble a six arms starfish, these starfish are built up from Gd(Y) d -states,

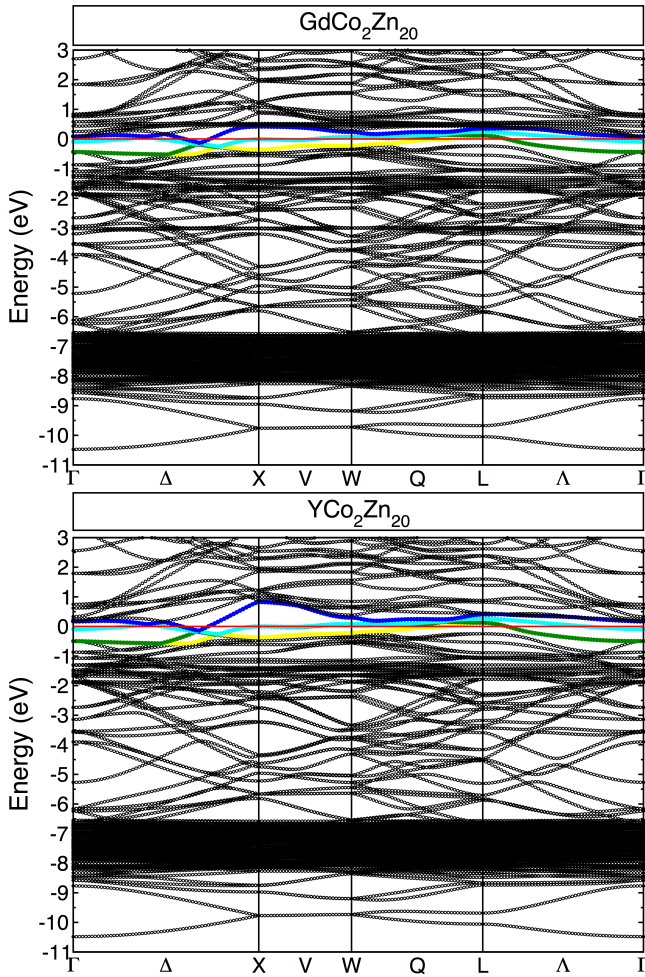


FIG. 8: Calculated dispersion relations for the $\text{GdCo}_2\text{Zn}_{20}$ (upper) and $\text{YCo}_2\text{Zn}_{20}$ (lower) systems. Highlighted in colors are the four conduction bands crossing the Fermi level; band 1 (yellow), band 2 (green), band 3 (cyan) and band 4 (blue). The eigenvalues are shifted with respect to the Fermi level, which is indicated by a red line.

Co d -states and Zn p and d -states. The third branch has one sphere at the center of the first Brillouin zone which is made up from Zn s -states and six structures that have the appearance of mushrooms with the stem along the Δ direction, this six mushrooms are formed from Gd(Y) d -states and Co d -states. The fourth branch is constituted of six lenses with their surfaces perpendicular to the Δ direction, these lenses are built up from Co d -states and Zn p -states.

For $\text{GdCo}_2\text{Zn}_{20}$ our calculations estimate a total DOS at the Fermi level of 3.03(1) states/f.u., spin and eV (Fig. 10). Similarly, a total DOS at the Fermi level of 3.02(1) states/f.u., spin and eV was estimated for the $\text{YCo}_2\text{Zn}_{20}$ (Fig. 10), which is comparable to the above values obtained experimentally. These results support the previous statement that $\text{YCo}_2\text{Zn}_{20}$ may be considered as an intermetallic compound with negligible electron-

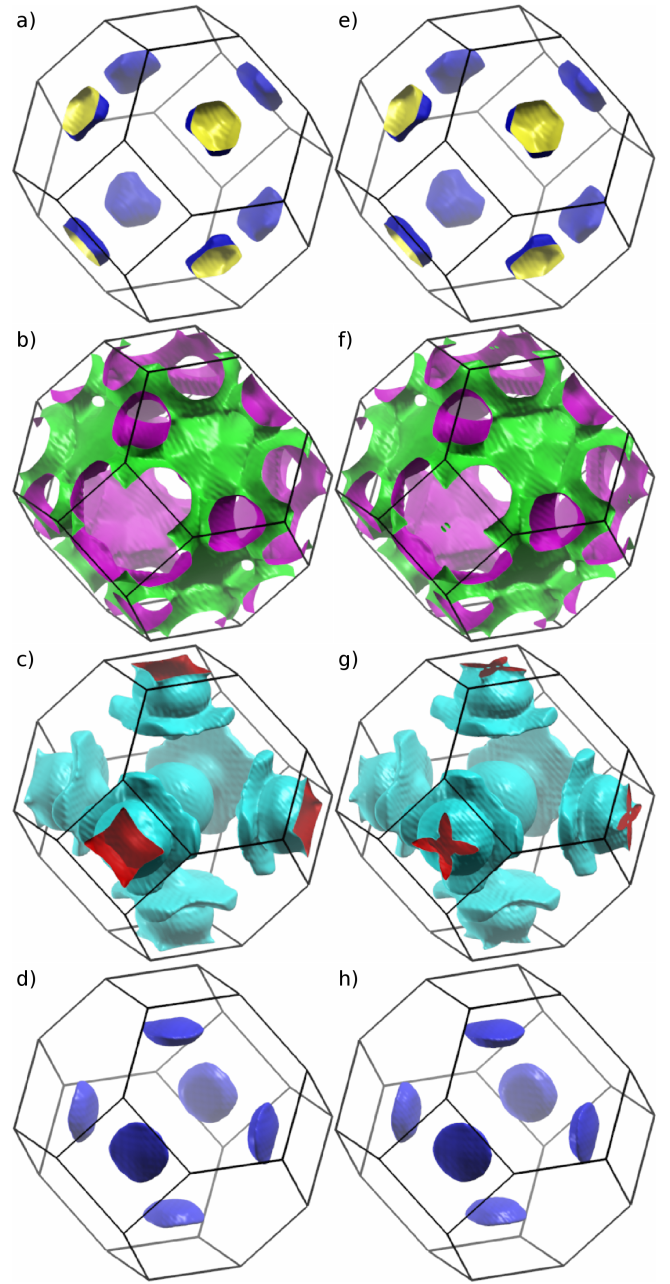


FIG. 9: Calculated Fermi surface for the $\text{GdCo}_2\text{Zn}_{20}$ and $\text{YCo}_2\text{Zn}_{20}$ systems. The four branches for $\text{GdCo}_2\text{Zn}_{20}$ corresponding to band 1, band 2, band 3 and band 4 are shown in (a), (b), (c) and (d), respectively. In the same manner, the four branches of $\text{YCo}_2\text{Zn}_{20}$ are shown in (e), (f), (g) and (h).

electron correlations, i.e. $\chi = \chi_0/(1 - \xi)$ with $\xi \ll 1$.

With all these details in mind, we now return to the ESR analysis. The exchange interaction, $\mathcal{H} = -J_{fs}\vec{S}_f \cdot \vec{s}_{ce}$ between the localized $4f$ -electron spin of Gd^{3+} , \vec{S}_f , and the ce of the $\text{YCo}_2\text{Zn}_{20}$, \vec{s}_{ce} , yields an ESR g -shift, Δg ,²⁹ and thermal broadening of the linewidth, b , (Korringa rate)¹¹ given by:

$$\Delta g = J_{fs}(0)\eta_F \quad (2)$$

and

$$b = \frac{d(\Delta H)}{dT} = \frac{\pi k_B}{g\mu_B} J_{fs}^2(0)\eta_F^2 = \frac{\pi k_B}{g\mu_B} (\Delta g)^2, \quad (3)$$

where $J_{fs}(0)$ is the effective exchange parameter in the absence of ce momentum transfer, i.e., $\langle J_{fs}(q) \rangle_F = J_{fs}(0)$,³¹ η_F is the “bare” density of states for one spin direction at the Fermi surface, k_B is the Boltzmann constant, μ_B is the Bohr magneton, and g is the Gd^{3+} g -value.

The above equations are normally used in the analysis of the ESR data in the limit of very diluted rare earths and concentration-independent g and b parameters, i.e., in the *unbottleneck* regime, absence of ce momentum transfer and single band compounds.³² Using the data in Table I and Eq. 3 one can observe that the correlation between g -shift, Δg , and b is only verified for the lowest Gd concentration samples. Moreover, Fig. 4, Fig. 5 and Table I show clear concentration-dependent ESR parameters, so our data must be analyzed in a different manner.

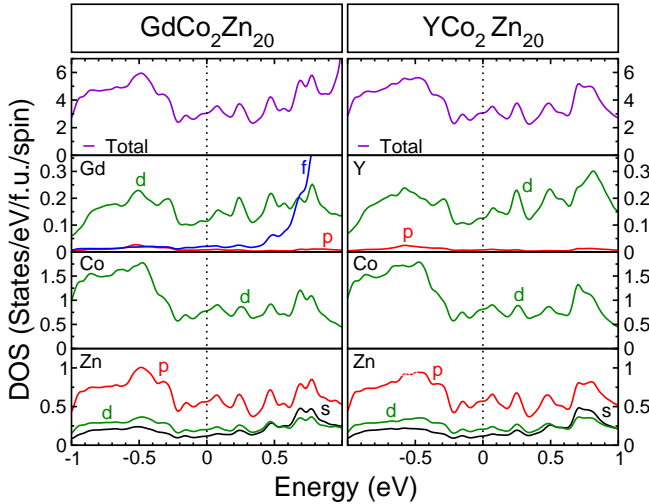


FIG. 10: Calculated total and partial DOS for $\text{GdCo}_2\text{Zn}_{20}$ and $\text{YCo}_2\text{Zn}_{20}$. The Fermi level is indicated by a dotted line.

The change of the Gd^{3+} g -shift from positive values (at low Gd concentrations) to negative ones (at high Gd concentrations) and the x -dependence of the Gd^{3+} ESR thermal broadening of the linewidth, b , (see Fig. 3 and Fig. 5) lead us to conclude that the relaxation of the Gd^{3+} ions to the lattice is processed via an exchange interaction, $J(\vec{S}_f \cdot \vec{s}_{ce})$, between the Gd^{3+} localized magnetic moment and different types of ce at the Fermi level.

In a multiband approximation the g -shift, Δg , and thermal broadening of the linewidth, b , are given by:

$$\begin{aligned} \Delta g &= \Delta g_{fs} + \Delta g_{fp} + \Delta g_{fd} \\ &= J_{fs}(0)\eta_{F_s} - J_{fp}(0)\eta_{F_p} + J_{fd}(0)\eta_{F_d} \end{aligned} \quad (4)$$

and

$$\begin{aligned} b &= \frac{\pi k_B}{g\mu_B} [F_s \Delta g_{fs}^2 + F_p \Delta g_{fp}^2 + F_d \Delta g_{fd}^2] \\ &= \frac{\pi k_B}{g\mu_B} [F_s \langle J_{fs}^2(q) \rangle_F \eta_{F_s}^2 + F_p J_{fp}^2(0) \eta_{F_p}^2 + F_d J_{fd}^2(0) \eta_{F_d}^2], \end{aligned} \quad (5)$$

where k_B is the Boltzmann constant, μ_B the Bohr magneton, and g the Gd^{3+} g -value; $J_{fi}(0)$ ($i = s, p, d$) are the effective $q = 0$ components of the exchange interaction between the Gd^{3+} $4f$ magnetic moment and the s -, p - and d -type ce ; η_{F_i} ($i = s, p, d$) the partial bare DOS (states/f.u., spin and eV) at the Fermi level of the s -, p - and d -type ce ; $\langle J_{fs}^2(q) \rangle_F$ is the average over the Fermi surface of the square of the q -dependent effective exchange parameter in the presence of ce momentum transfer, $q = |\vec{k}_{out} - \vec{k}_{in}|$, i.e., $\langle J_{fs}(q) \rangle_F \neq J_{fs}(0)$;³¹ $F_s = 1$, $F_p = 1/3$ and $F_d = 1/5$ are factors associated with the orbital degeneracy of the unsplit (no crystal field effects) bands at the Fermi level, respectively. The q -dependence of the exchange interaction with the p -type and d -type ce will be considered constant over the Fermi surface, i.e., $\langle J_{fp,d}(q) \rangle_F = J_{fp,d}(0)$ (see below).

In Eq. 4 we have considered that the contribution to Δg due to the exchange interaction with s - and d -type ce are positive (atomic-like) and that with p -type ce is negative (covalent-like).³¹

Due to the strong spin-orbit coupling of p - and d -type ce compared to that of the s -type ce , we assume that only the s -type ce are capable of experiencing the *bottleneck* effect. Hence, we can consider that the contribution to the ESR parameters, g -shift and b , of the s -type ce are negligible in the highly concentrated samples. With these assumptions, for $x = 1$ ($\text{GdCo}_2\text{Zn}_{20}$, extreme *bottleneck*) Eq. 4 reduces to

$$\Delta g = -0.002(2) = -J_{fp}(0)\eta_{F_p} + J_{fd}(0)\eta_{F_d}, \quad (6)$$

and Eq. 5 reduces to (see Fig. 10b):

$$b = 1.9(6) \text{ Oe/K} = \frac{\pi k_B}{g\mu_B} [F_p J_{fp}^2(0) \eta_{F_p}^2 + F_d J_{fd}^2(0) \eta_{F_d}^2]. \quad (7)$$

In general, the q -dependence of the exchange parameters $J_{f,i}$ ($i = s, p, d$) cannot be disregarded, but in

the case in which the relaxation rate, b , scales or is slightly larger than the expected value from the g -shift ($b = (\pi k_B / g \mu_B) (\Delta g)^2$) we can neglect the q -dependence of the J_{fp} and J_{fd} exchange parameters. In our case, we have that $1.9 \text{ Oe/K} \geq (\sim 2.34 \times 10^4 \text{ Oe/K}) \times (-0.002)^2 \approx 0.1 \text{ Oe/K}$ in agreement with Table I.

From Fig. 10 for $\text{GdCo}_2\text{Zn}_{20}$, we have $\eta_{F_d} = 1.09(1)$ states/f.u., spin and eV and $\eta_{F_p} = 0.59(1)$ states/f.u., spin and eV. Then, using Eqs. 6 and 7 we estimate $J_{fd}(0) = 10(5) \text{ meV}$ and $J_{fp}(0) = 22(6) \text{ meV}$.

Conversely, in the *unbottleneck* regime (lowest Gd concentration, $x \approx 0.002$), and from Fig. 10 for $\text{YCo}_2\text{Zn}_{20}$, Eqs. 4 and 5 reduce to:

$$\Delta g = 0.019(2) = J_{fs}(0)\eta_{F_s} - 0.002(2), \quad (8)$$

$$b = 8.6(6) \text{ Oe/K} = \frac{\pi k_B}{g \mu_B} [F_s \langle J_{fs}^2(q) \rangle_F \eta_{F_s}^2] + 1.9(6). \quad (9)$$

Again from Eqs. 8 and 9 and using $\eta_{F_s} = 0.13(1)$ states/f.u., spin and eV, we obtain $J_{fs}(0) = 167(7) \text{ meV}$ and $\langle J_{fs}^2(q) \rangle_F^{1/2} = 18(5) \text{ meV}$. Comparing this value with those for $J_{fp}(0)$ and $J_{fd}(0)$, we find that in these compounds the polarization component of the exchange parameter $J_{fs}(0)$ is an order of magnitude larger.

Thus, in order to describe the antiferromagnetic ordering of $\text{GdCo}_2\text{Zn}_{20}$, it should be more appropriate to use an RKKY approach that considers only the exchange parameter $J_{fs}(0)$ (due to the delocalized nature of the s -type electrons compared with p and d -type) rather than the Campbell model,^{34,35} that considers the $J_{fd}(0)$ term as the most important one. Therefore our obtained value in ESR considerations for $J_{fs}(0)$ will be used to correlate with the RKKY interaction that is only true in very dilute magnetic systems as this family of compounds.

It is known that in general, the RKKY interaction depends strongly of the Fermi surface and can have different analytical forms for each case. Finding a suitable expression for a real material with a complex Fermi surface is thus expected to be an almost impossible task. The equation that represents a generalized form of the RKKY interaction is given by³⁶:

$$J_{RKKY} \sim J_{fs}^2 \sum_{\mathbf{k}, \mathbf{q}} \frac{f_{\mathbf{k}} - f_{\mathbf{k}+\mathbf{q}}}{\epsilon(\mathbf{k} + \mathbf{q}) - \epsilon(\mathbf{k})}, \quad (10)$$

where $f_{\mathbf{k}} = \Theta(k_F - |\mathbf{k}|)$ and $f_{\mathbf{k}+\mathbf{q}} = \Theta(k_F - |\mathbf{k} + \mathbf{q}|)$ are the step functions that come from the non-zero matrix elements, according to the second-order perturbation theory treatment of the second quantized Heisenberg hamiltonian, between a localized and an itinerant electron spin coupled by J_{fs} . The therm $\epsilon(\mathbf{k} + \mathbf{q}) - \epsilon(\mathbf{k})$ corresponds to the energy difference between the ground state and

the excited state. This function is known as a Lindhard function that appears in the generalized form of the magnetic susceptibility³⁶. Transforming the two summations into integrals, one may reach the actual expression for the RKKY interaction. Our calculated Fermi surface, shown in Fig. 9, evidences a rather complex dispersion relation for the $\text{GdCo}_2\text{Zn}_{20}$ compound, so obtaining an exact analytical solution from Eq. 10 is not possible.

However, within a simple Fermi gas model ($\epsilon(\mathbf{k}) \sim k^2$) the problem is simplified and more accessible. In this approximation the analytical expression of the RKKY interaction for the effective coupling between two lattice localized spins is given, in terms of k_F , by³⁸:

$$J_{eff} \approx \frac{9\pi(J_{fs}(0))^2 \nu^2 F(r)}{64E_F(2k_F)^4}, \quad (11)$$

where ν is the number of conduction electrons per atom, E_F the Fermi energy, $J_{fs}(0)$ the coupling constant between the Gd^{3+} spin S_f and the conduction electron spin s_{ce} , ($\mathcal{H} = -J_{fs}(0)\vec{S}_f \cdot \vec{s}_{ce}$), and $F(r)$ is the RKKY function given by:

$$F(r) = \frac{\sin(2k_F r) - 2k_F r \cos(2k_F r)}{r^4}. \quad (12)$$

Hence, in the $\text{GdCo}_2\text{Zn}_{20}$ compound, it is possible to estimate the effective exchange parameter, J_{eff} (Eq. 11), due to the coupling between two nearest Gd^{3+} neighbors via the damped spin polarization of only the s -type ce , as it can be observed in the third branch of the Fermi surface (Fig. 9 (c,g)).

For $\text{GdCo}_2\text{Zn}_{20}$ the following band structure parameters were determined from the DFT calculations: $E_F = 3.77 \text{ eV}$ with $k_F = 0.99478 \times 10^{10} \text{ m}^{-1}$ ($k_F = \frac{1}{\hbar} \sqrt{2m_e E_F}$) and $\nu = 1.23 \text{ c.e./atom}$. Notice that the value of $k_F = 0.99478 \times 10^{10} \text{ m}^{-1}$ is comparable to those reported for uncorrelated simple metals such as Cu, Ag and Au.³⁷ Then, the amplitude of the RKKY function $F(r)$ at $r = 6.0 \text{ \AA}$ (nearest Gd-Gd neighbors) gives $F(6.0 \text{ \AA}) = -7.99 \times 10^{37} \text{ m}^{-4}$ (Fig. 11) and, consequently, $J_{eff} \approx -25.2(7) \times 10^{-4} \text{ meV}$, a negative value as expected for antiferromagnetic ordering.

Now, a *microscopic* Curie-Weiss temperature estimation can be made from this result using the formula given by Coey:³⁸

$$\theta_C = \frac{2Z J_{eff} S(S+1)}{3k_B}, \quad (13)$$

with $Z = 4$ (Gd nearest neighbors in $\text{GdCo}_2\text{Zn}_{20}$) and $S = 7/2$ for Gd^{3+} . We obtain $\theta_C = -1.2(2) \text{ K}$ which is, within the accuracy of our experiments, in very good agreement with the *bulk* estimation (Fig. 7) extracted from the magnetic susceptibility measurements.

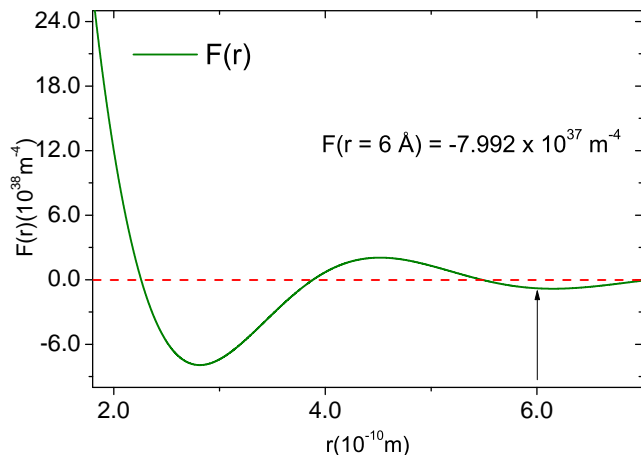


FIG. 11: RKKY oscillatory coupling function $F(r)$ as a function of distance r between Gd ions. The arrow indicates the Gd-Gd separation in the $\text{GdCo}_2\text{Zn}_{20}$ system.

V. CONCLUSIONS

Our experimental ESR results of $\text{Y}_{1-x}\text{Gd}_x\text{Co}_2\text{Zn}_{20}$ ($0.002 \lesssim x \leq 1.00$) were analyzed within a multiband model of ce (s -, p - and d -type) where, via the Gd concentration, the system was tuned from an *unbottleneck* regime ($\text{Y}_{0.998}\text{Gd}_{0.002}\text{Co}_2\text{Zn}_{20}$) to a *bottleneck* regime ($\text{GdCo}_2\text{Zn}_{20}$). The combination of ESR results with those of heat capacity, magnetic susceptibility and band structure calculations allowed us to estimate the polarization component of the exchange parameters, $J_{fi}(0)$ ($i = s, p, d$). Besides, by the assumption that only the s -type of ce can experience the *bottleneck* effect, due to their relatively weak spin-orbit coupling, we found that the average over the Fermi surface of the exchange param-

eter, associated to the ce momentum transfer, is different from the exchange parameter leading to local polarization effects, i.e., $\langle J_{fs}(q) \rangle_F \neq J_{fs}(0)$.

The exchange parameters obtained with this multiband scenario revealed that $J_{fs}(0)$ is dominant over $J_{fp}(0)$ and $J_{fd}(0)$. This allowed a tractable RKKY description for the antiferromagnetic behavior of the $\text{GdCo}_2\text{Zn}_{20}$ compound. Despite the fact that these compounds are structurally complex, we found that under certain reasonable approximations and using the combination of different experimental results with DFT calculations, the RKKY approach gave a very good quantitative description of the magnetic interaction, as expected for a naturally diluted structure of rare-earth ions. This was confirmed by the reasonably accurate prediction of the Curie-Weiss temperature in terms of microscopic parameters.

With the resulting establishment of $\text{GdCo}_2\text{Zn}_{20}$ as a model RKKY system, we expect that this work can provide key reference elements to help understand the behaviors of related materials such as $\text{RFe}_2\text{Zn}_{20}$ and $\text{YbT}_2\text{Zn}_{20}$, with their more complex and remarkable electronic and magnetic properties.

Acknowledgments

This work was supported by Brazilian agencies FAPESP (Grant Nos. 2011/19924-2, 2012/17562-9), CNPq, FINEP and CAPES. We thank R. A. Ribeiro for sample preparation support and P. G. Pagliuso for fruitful discussions. JMOG would like to thank CODI-Vicerrectoria de Investigación-Universidad de Antioquia.

-
- ¹ S. Jia, N. Ni, S. L. Bud'ko, and P. C. Canfield, Phys. Rev. B **76**, 184410 (2007).
 - ² S. Jia, N. Ni, S. L. Bud'ko, and P. C. Canfield, Phys. Rev. B **80**, 104403 (2009).
 - ³ T. Nasch, W. Jeitschko, and U. C. Rodewald: Z. Naturforsch. B **52**, 1023 (1997).
 - ⁴ S. Jia, N. Ni, G. D. Samolyuk, A. Safa-Sefat, K. Dennis, H. Ko, G. J. Miller, S. L. Bud'ko, and P. C. Canfield, Phys. Rev. B **77**, 104408 (2008).
 - ⁵ S. Jia, S. L. Bud'ko, G. D. Samolyuk, and P. C. Canfield, Nat. Phys. **3**, 334 (2007).
 - ⁶ M. S. Torikachvili, S. Jia, E. D. Mun, S. T. Hannahs, R. C. Black, W. K. Neils, Dinesh Martien, S.L. Bud'ko, and P. C. Canfield, Proc. Natl. Acad. Sci. U.S.A. **104**, 9960 (2007).
 - ⁷ T. Tanaka, and Y. Kubo, J. Phys. Soc. Jpn. **79**, 124710 (2010).
 - ⁸ R. H. Taylor, Adv. Phys. **24**, 681 (1975).
 - ⁹ S. E. Barnes Adv. Phys. **30**, 801 938 (1981).
 - ¹⁰ H. Hasegawa, Prog. Theor. Phys. **21**, 1752 (1968).
 - ¹¹ J. Koringa, Physica **16**, 601 (1950).
 - ¹² D. Davidov, A. Chelkowski, C. Rettori, R. Orbach, and M. B. Maple, Phys. Rev. B **7**, 1029 (1973).
 - ¹³ C. Rettori, H. M. Kim, E. P. Chock, and D. Davidov, Phys. Rev. B **10**, 1826 (1974).
 - ¹⁴ C. Rettori, D. Davidov, R. Orbach, E. P. Chock, and B. Ricks, Phys. Rev. B **7**, 1 (1973).
 - ¹⁵ M. Cabrera-Baez, W. Iwamoto, E. T. Magnavita, J. M. Osorio-Guillén, R. A. Ribeiro, M. A. Avila and C. Rettori, J. Phys. Cond. Mat. **26**, 175501 (2014).
 - ¹⁶ R. A. Ribeiro and M. A. Avila, Phil. Mag. **92**, 2492 (2012).
 - ¹⁷ P. C. Canfield and Z. Fisk, Phil. Mag. **65**, 1117 (1992).
 - ¹⁸ A. R. Denton and N. W. Ashcroft, Phys. Rev. A **43**, 3161 (1991).
 - ¹⁹ V. A. Ivanshin, T. O. Litvinova, A. A. Sukhanov, N. A. Ivanshin, S. Jia, S. L. Bud'ko and P. C. Canfield, JETP Letters **99**, 3 (2014).
 - ²⁰ J.P. Perdew, A. Ruzsinszky, G.I. Csonka, O.A. Vydrov, G.E. Scuseria, L.A. Constantin, X. Zhou, and K. Burke, Phys. Rev. Lett. **100**, 136406 (2008).

- ²¹ G. Kresse and J. Furthmüller. Phys. Rev. B **54**, 11169 (1996).
- ²² G. Kresse and D. Joubert. Phys. Rev. B **59**, 1758 (1999).
- ²³ K. Dewhurst, S. Sharma, L. Nordström, and H. Gross, URL <http://elk.sourceforge.net>.
- ²⁴ A. Kokalj, Comp. Mater. Sci., 2003, Vol. 28, p. 155
- ²⁵ A. Abragam and B. Bleaney, Electron Paramagnetic Resonance (EPR) of Transition Ions (Oxford: Clarendon)(1970).
- ²⁶ G. Feher and A. F. Kip, Phys. Rev. **98**, 337 (1955).
- ²⁷ F. J. Dyson, Phys. Rev. **98**, 349 (1955).
- ²⁸ C. P. Jr. Poole, Electron Spin Resonance: A Comprehensive Treatise on Experimental Techniques (New York: Wiley) pp 705-17 (1969).
- ²⁹ K. Yosida, Phys. Rev. **106**, 893 (1957).
- ³⁰ K. Wakiya, T. Onimaru, S. Tsutsui, K. T. Matsumoto, N. Nagasawa, A. Q. R. Baron, T. Hasegawa, N. Ogita, M. Udagawa and T. Takabatake, arXiv:cond-mat/1410.7916.
- ³¹ D. Davidov, K. Maki, R. Orbach, C. Rettori, and E. P. Chock, Solid State Commun.**12**, 621 (1973).
- ³² D. Davidov, R. Orbach, C. Rettori, D. Shaltiel, L. J. Tao, and B. Ricks, Phys. Lett.**35A**, 339 (1971).
- ³³ P. F. S. Rosa, L. A. S. de Oliveira, C. B. R. de Jesus, K. O. Moura, C. Adriano, W. Iwamoto, T. M. Garitezi, E. Granado, M. E. Saleta, K. R. Pirola, P. G. Pagliuso, Solid State Commun.**191**, 14-18 (2014).
- ³⁴ I. A. Campbell, J. Phys. F: Met. Phys. **2** L47 (1972).
- ³⁵ H. S. Li, Y. P. Li and J. M. D. Coey, J. Phys. Cond. Mat. **3**, 7277-7290 (1991).
- ³⁶ J. Jensen and A. R. Mackintosh, Rare Earth Magnetism, (Oxford: Clarendon) (1991).
- ³⁷ N. W. Ashcroft and N.D. Mermin, Solid State Physics, Saunders, (1976).
- ³⁸ J. M. D. Coey, Magnetism and Magnetic Materials (Cambridge) (2009).